ChemistrySelect

Research Article
doi.org/10.1002/slct.202201374

Chemistry Europe
European Chemical Societies Publishing

www.chemistryselect.org

Inorganic Chemistry

Multimodal Imaging Contrast Property of Nano Hybrid Fe_3O_4@Ag Fabricated by Seed-Growth for Medicinal Diagnosis

The Tam Le,*[a] Thi Ngoc Linh Nguyen,*[b] Hoa Du Nguyen,[a] Thi Hong Tuyet Phan,[a] Hong Nam Pham,[c, f] Duc Giang Le,[a] Thanh Phong Hoang,[d] Thi Quynh Hoa Nguyen,[a] Trong Lu Le,[e, f] and Lam Dai Tran[e, f]

Multimodal imaging, which integrates different imaging modalities, is emerging as a promising strategy to improve both preclinical and subclinical imaging. Computed tomography (CT) and magnetic resonance imaging (MRI) are among the imaging techniques widely used in clinical practice. These imaging modalities are used to diagnose and screen disease, each providing additional and different information about the patient and pathosis. In this research, we present the development of a model that combines a hybrid nanostructure, consisting of an iron oxide core and a silver-shell nanoparticle for dual MRI/CT imaging. Fe_3O_4@Ag HNPs with core-shell structure were fabricated by reducing Ag^+ on the surface of Fe_3O_4 (NPs) nanoparticles by seed-growth route in the thermal decomposition method. TEM images show that the synthesized nanoparticles have a uniform spherical shape and size, with an average diameter of 15.6 nm. The hybrid nanoparticles after functionalizing the surface with polyacrylic acid (PAA) became hydrophilic and dispersed well in water. The fluid of Fe_3O_4@Ag@PAA HNPs has high stability in water media with NaCl salt concentrations above 200 mM and a wide pH range from 4 to 11. The fluid Fe_3O_4@Ag@PAA has selective cytotoxicity with IC_{50} value 8.42 ug/ml for Hep-G2 cell lines, and 40.3 ug/ml for normal Vero cell lines. The results of in-vitro MRI/CT imaging showed that the value of transverse relaxation rate r_2 was 138.6 $mM^{-1}s^{-1}$ and had good X-ray attenuation ability. With these outstanding properties, the core-shell structured nano hybrid fluid presented in this research has the potential as a candidate for multimodal bioimaging techniques in practical applications.

1. Introduction

Recently, technological advances have directly impacted the medical imaging diagnosis field. Magnetic resonance imaging (MRI) and computed tomography (CT) are diagnostic imaging techniques used most commonly in medicine today due to three-dimensional space resolution, good image quality and deep penetration of electromagnetic waves into the body without surgery.[1–4] However, the main limitation of these diagnostic techniques is their relatively low sensitivity, so many cases require the use of contrast agents to improve image quality.[5,6] In clinical MRI studies, the positive contrast agent T_1 commonly used is based on the complex substances of paramagnetic Gd^{3+} with 7 unpaired electrons 4f that create a large magnetic moment (7.94 μB).[7–11] These complex substances have linear or cyclic structures such as gadopentetate (trade name is Magnevist), gadobenate (Multihance), gadodiamide (Omniscan), gadoteridole (Prohance), or gadobutrol (Gadovist).[9] Although Gd is considered safe when used as a chelated compound, the use of some chelates Gd in people with kidney disease has been linked to a rare but serious complication called "nephrogenic systemic fibrosis". Many renal and pancreatic side effects commonly encountered in patients using contrast agents in the form of Gd^{3+} complexes have been reported[13–16] For this reason, the World Health Organization (WHO) has issued a restriction on the use of Gd contrast agents. Furthermore, due to their low molecular weight, Gd complex-based contrast agents are usually the most non-specific extracellular contrast agents and exhibit rapid clearance from the vascular compartment.[14–17]

Because contrast agents (contrasts) used for CT are substances that cause attenuation of X-ray radiation by

[a] Dr. T. T. Le, Prof. H. D. Nguyen, Prof. T. H. T. Phan, Prof. D. G. Le, Prof. T. Q. H. Nguyen
Vinh University, 182 Le Duan, Vinh City 460000, Vietnam
E-mail: tamlt@vinhuni.edu.vn
[b] Dr. T. N. L. Nguyen
Thai Nguyen University of Sciences, Tan Thinh Ward, Thai Nguyen City 250000, Vietnam
E-mail: linhntn@tnus.edu.vn
[c] Dr. H. N. Pham
Institute of Materials Science, Vietnam Academy of Science and Technology, 18 Hoang Quoc Viet Road, Hanoi 100000, Vietnam
[d] Dr. T. P. Hoang
Department of Education and Training in Nghe An, 67 Nguyen Thi Minh Khai, Vinh City 460000, Vietnam
[e] Dr. T. L. Le, Prof. L. D. Tran
Institute for Tropical Technology, Vietnam Academy of Science and Technology, 18 Hoang Quoc Viet Road, Hanoi 100000, Vietnam
[f] Dr. H. N. Pham, Dr. T. L. Le, Prof. L. D. Tran
Graduate University of Science and Technology, Vietnam Academy of Science and Technology, 18 Hoang Quoc Viet Road, Hanoi 100000, Vietnam

Supporting information for this article is available on the WWW under https://doi.org/10.1002/slct.202201374

absorbing or scattering X-rays, the compounds of elements that have large Z nuclei or high-density materials are used.[18–22] Currentlyiodine complexes such as Iohexol (Omnipaque trade name), Iodixanol (Visipaque), or Iversol (Iversol) are commonly used in the world. However, these complex substances also cause a lot of side effects such as skin allergies, abnormal heart rhythms, dyspnea and are especially contraindicated for patients with kidney disease, even in some cases, it can be fatal due to anaphylactoid shock.[23] Furthermore, iodinated contrast agents approved by FDA (Food and Drug Administration) can be removed very quickly from the blood and are not convenient for diseases that take a long time to diagnose.[24] For about the last two decades there have been no new approved CT contrast agents, while many contrast agents for PET, SPECT, MR imaging have been developed and approved, despite many studies of gold nanoparticles (Au NPs) as CT contrast agents are performed. Au NPs have many favorable properties for this application such as a large payload of contrast material, strong X-ray attenuation, adjustable material size and shape, high biocompatibility, mutable chemical surface used.[18–22] However, one disadvantage of Au NPs-based contrast agent is its high cost.

Meanwhile, magnetic nanoparticles are promising materials in clinical research, especially in the fight against cancer through several applications such as drug-carrying agents, hyperthermia, and MRI imaging diagnosis agent.[25–27] Besides, Ag NPs have many useful biological features, such as antibacterial, antiviral, and antifungal.[28–30] The unique optical properties of Ag NPs have also been applied to the development of sensors, imaging agents, and clinical treatment.[31,32] Ag nanoparticles can replace Au because it is cheaper and has a large enough X-ray attenuation coefficient. The gray levels in the CT slice images correspond to X-ray attenuation, reflecting the proportion of X-rays scattered or absorbed as they pass through each voxel and are influenced by the density and composition of the material being taken the photo. Thus, using Ag NPs is speculated to attenuate X-rays and help the CT images clearer with higher contrast than iodine complexes. However, there are still some obstacles that need to be studied further, such as cytotoxicity, targeting, and controlled ability. On the other hand, in order to overcome the limitations of separated imaging diagnosis methods, the development of multimodal imaging techniques (CT/MRI) is interesting, leading to a need for multimodal contrast agents.[33–36] The idea of hybridization two types of nanoparticles (Fe_3O_4@Ag hybrid NPs) has been proposed as a solution to overcome this problem. The integration of nanomaterials with different properties in a suitable nanostructure of the hybrid materials makes them not only possess the characteristic properties of each composite component, but it is also possible to improve those properties or to have new characteristics due to the interaction between the components.[37–39]

In this study, we use the seeded-growth method to fabricate the hybrid Fe_3O_4@Ag NPs with poly (acrylic acid) (PAA) as a hydrophilic layer for dispersion of the materials in water. The obtained Fe_3O_4@Ag hybrid NPs materials were initially evaluated with the dual contrast property as an agent for multimodality imaging MRI/CT techniques. The cytotoxicity testing results on Vero and Hep G2 cell lines showed that they were toxic to cancer cell lines in comparison with normal cells.

2. Results and discussion

2.1. The formation of Fe_3O_4 NPs and Fe_3O_4@Ag hybrid NPs

The fabrication of the hybrid structure materials between Fe_3O_4 and Ag for the biological application takes three steps as depicted in (Scheme 1). In the reaction mixtures, oleate anion

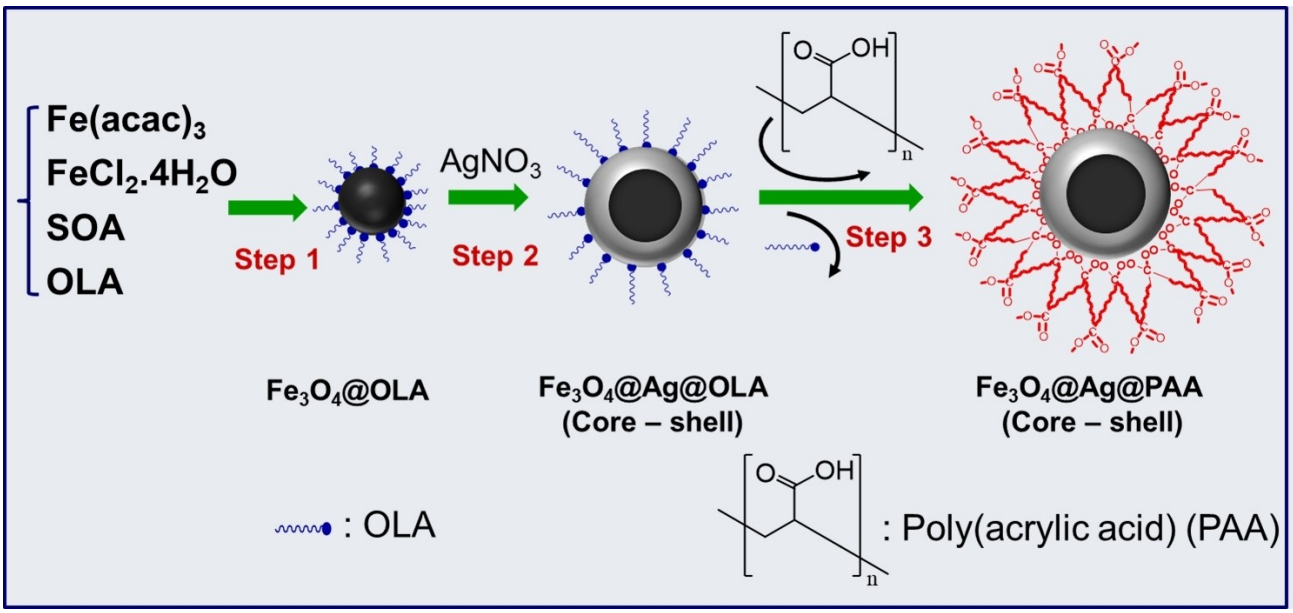

Scheme 1. Schematic three steps of the fabrication of Fe_3O_4@Ag@PAA hybrid nanoparticles.

may acts as a ligand to form the intermediate complexes with Fe(II) and Fe(III). The changes in morphology and size of particles at different concentrations of SOA from 300–750 mM were investigated and the results demonstrated the influence of SOA (Figure 1). At the concentrations of 300 mM and 750 mM the Fe_3O_4 particles are small but non-uniform, with an average particle size of 6.1 ± 1.2 nm and 12.3 ± 1.6 nm, respectively (Figure 1a). When increasing the SOA concentration to 450 mM, Fe_3O_4 NPs were obtained uniformly, with an average size of 8.1 ± 0.8 nm, the particle size error in this case decreased, reaching ≈ 10% (Figure 1b). With the sample with SOA concentration of 600 mM, non-uniform Fe_3O_4 nanoparticles with various shapes such as sphere, triangle and cube were obtained with the average size increasing and reaching 12.3 ± 1.6 nm, size error particles in this case are 13% (Figure 1c). With the 750 mM sample, mainly Fe_3O_4 nanoparticles were obtained with a cubic shape with an average size of 15.6 ± 2.1 nm, the particle size error in this case was 13.5% (Figure 1d). At the concentrations of 450 mM, with Fe/SOA ratio 1 : 2.5 (concentration value 180 mM for Fe, and 450 mM for SOA, respectively), Fe_3O_4 NPs were obtained uniformly, it can be explained with the mechanism of Fe_3O_4 formation through the bridged or polynuclear complex Fe(III)-Fe(II)-Fe(III) (Figure 1g). Thus, when SOA concentration increases, the particle size increases and the shape of Fe_3O_4 nanoparticles changes markedly (Figure 1e, f).

The increase in the size of Fe_3O_4 NPs with increasing SOA concentration may be due to the influence of iron oleate

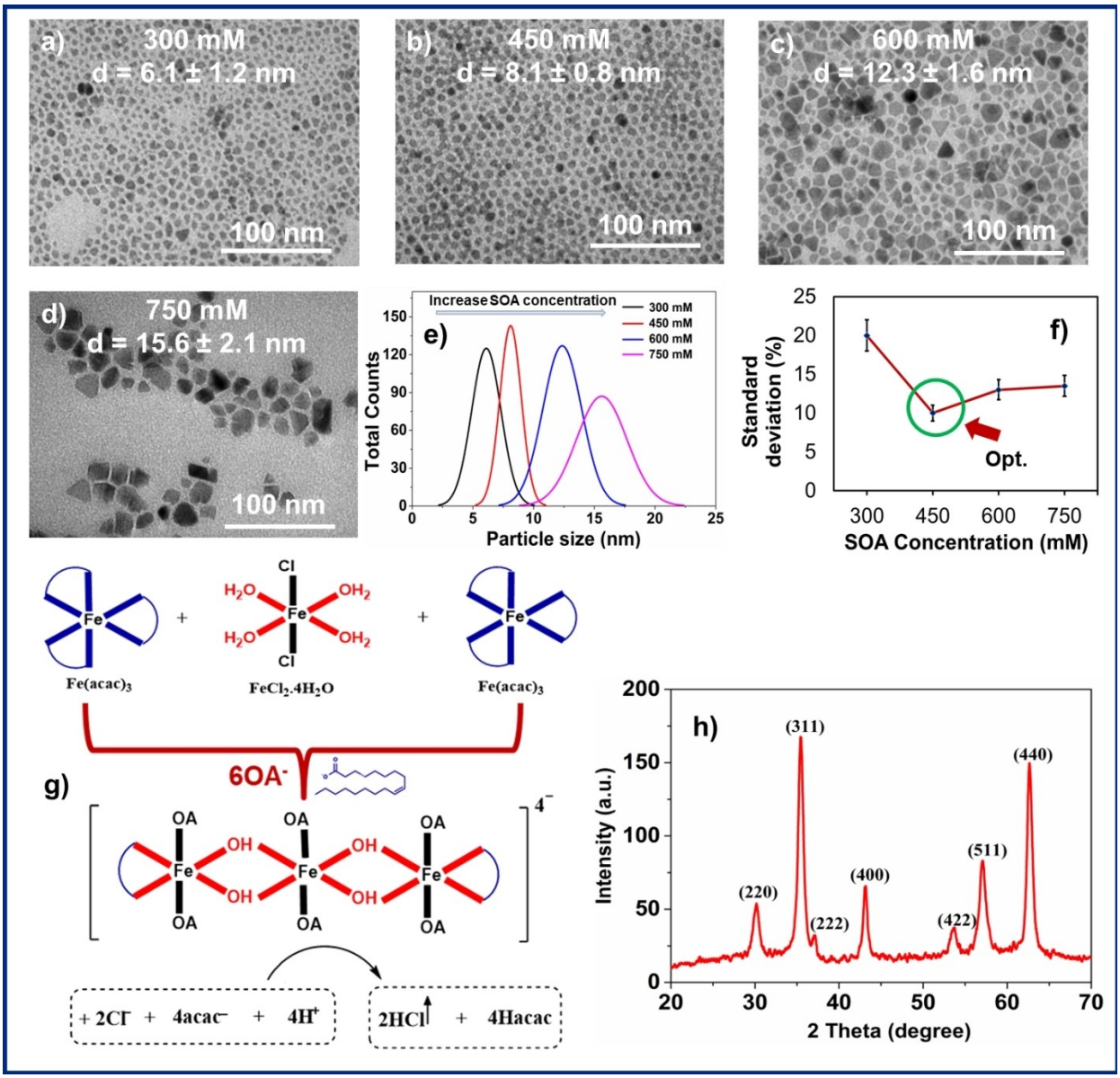

Figure 1. TEM images of the Fe_3O_4 NPs (a-d) and their histogram of particle size distribution synthesised at different concentrations of SOA (e) ; The standard deviation (SD) of particle size at different concentrations of SOA (f); mechanism of Fe_3O_4 formation through the bridged or polynuclear complex Fe(III)-Fe(II)-Fe(III) (g) and Xray diffraction pattern of the Fe_3O_4 NPs prepared at the concentration of SOA 450 mM (h). (Scale bar: 100 nm).

complex (intermediate agent complex) in the synthesis process. Iron(III) acetylacetonate is decomposed at about 190 °C,[40] however, if they form complexes with OA for oleate complexes, their decomposiion temperature increases to about 300 °C.[41] When SOA concentration is low, the iron is mainly in the form of acetylacetonate complex, and will be quickly decomposed at a temperature of 230–250 °C to form crystal nuclei. Then, the source of iron will be reduced to feed the growth stage of these crystallites, resulting in nanoparticles will be smaller. On the other hand, according to the theory of crystallite growth, low concentrations of precursors with low reaction rates lead to Ostwald ripening, and are also the reason for the wide size distribution of Fe_3O_4 nanoparticles in samples with low SOA concentration.[42] When SOA concentration is high, iron(III) and iron(II) mainly form complexes with SOA to form oleate complexes. At the high decomposition temperature of the oleate complex, a source of iron is available in solution to facilitate the growth of crystallite. It results that larger sized nanoparticles are obtained. At high concentrations of SOA, in addition to the increased Fe_3O_4 particle size, there was also a shape change from sphere to triangle and cube, as in our previous research when synthesizing $CoFe_2O_4$ nanoparticles.[43]

The XRD pattern showed that the materials had diffraction peaks which corresponding to crystal planes (220), (311), (400), (422), (511) and (440) at positions of 30.16°; 35,49°; 43,01°; 53,78°; 57.21° and 62.73° (JCPDS, No. 19-0629), assigned to Fe_3O4's spinel structure. Figure 1h is an X-ray diffraction pattern of a representative Fe_3O_4 nanosample fabricated at a SOA concentration of 450 mM. The average crystal size obtained from the peak expansion (311) is 8.3 nm, which is consistent with the TEM image analysis results presented in Figure 1b as 8.1 ± 0.8 nm.

Figure 2 shows the TEM images and size distribution histograms of Fe_3O_4 nanoparticles and Fe_3O_4@Ag hybrid nanoparticles. The results indicate that the Fe_3O_4 NPs particles are spherical, monodisperse, uniform in size and shape with an average size of 8.1 ± 0.8 nm (Figure 2a). As shown in Figure 2b, the core-shell hybrid nanoparticles formed from the combination of Fe_3O_4 and Ag NPs (Fe_3O_4 @ Ag) have uniform size and shape with an average size of 15.2 ± 1.2 nm. This result can be explained based on the seed-mediated growth reaction, in which Ag atoms tend to be deposited on the surface of the seed Fe_3O_4 nanoparticles to minimize the energy. Then, the positions with the presence of Ag atoms become more active as nuclei for crystal growth by continuously deposition of Ag to form the Ag shell. Thus, the Ag shell is gradually formed through the formation of Ag nanocrystals.[44] In addition, energy dispersive X-ray spectroscopy (EDS) analysis of Fe_3O_4@Ag hybrid nanoparticles further confirmed the existence of Fe and Ag elements in the hybrid nanoparticles (Figure 2d). The Fe_3O_4@Ag hybrid nanostructure formation was also confirmed through UV-Vis absorption spectroscopy. As can be observed in Figure 2e, in the wavelength range 300–800 nm, the Fe_3O_4 NPs have no absorption peak, while the Fe_3O_4@Ag HNPs showed a surface plasmon resonance (SPR) peak at 411 nm, assigned to the Ag layer on the surface of Fe_3O_4 particles, which is consistent with the observed results from the TEM image. These results demonstrated that the obtained Fe_3O_4@Ag HNPs have core-shell structure.

The formation of Fe_3O_4@Ag hybrid core-shell structure was also demonstrated by X-ray diffraction method (Figure 2g), in which the diffraction peaks of Fe_3O_4 did not observe, but only the typical peaks for Ag face-centered cubic (fcc) structure at positions (2-theta) = 38.21°; 43.61° and 64.21° correspond to the lattice planes (111), (200) and (220) (JCPDS 004-0783). This proved that the Fe_3O_4 particles were completely covered by the Ag shell as observed in the TEM image in Figure 2b.

The chemical composition of the surface coating of the Fe_3O_4@Ag hybrid nanoparticles was characterized by FT-IR spectra as shown in Figure 3a. For the nanohybrid materials sample before phase transfer, two bands at 3469 and 3365 cm^{-1} and a weak band at 1624 cm^{-1} which are assigned to the stretching and bending vibrations of -NH_2 group, a weak band at 1556 cm^{-1} is assigned to C=C stretching, all confirmed the present of OLA molecule in the surface of Fe_3O_4@Ag hybrid nanoparticles. In the IR spectrum of the PAA-coated Fe_3O_4@Ag obtained by phase transfer with PAA, the broaden strong band at 3290 cm^{-1} and a strong band at 1635 cm^{-1} are assigned to OH and C=O stretchs of the –COOH group, showed the shift to lower frequency than that of free PAA, which confirmed the binding of PAA on the surface of Fe_3O_4@Ag hybrid nanoparticles.[27]

TGA curve of Fe_3O_4@Ag@OA/OLA materials (Figure 3b) showed two mass reduction steps. In the first step, the sample lost only about 2.6% by weight at temperatures between 90–250 °C, which can be assigned to organic solvents adsorbed on the surface of the materials. In the second step, the 4.6% mass loss occurring at a temperature range of 250–600 °C may be due to the loss of the OA/OLA surfactant molecules. Thus, it can be concluded that the remaining 92.8% weight is the weight of Fe_3O_4@Ag hybrid nanoparticles and 7.1% by weight is the organic coating of OA/OLA. In the TGA curve of the sample Fe_3O_4@Ag@PAA, the total mass loss of about 35.1% in which the first step about 2.7% due to loss H_2O on the hydrophilic surface in the range of 65 to 200 °C, and the second step in the range of 200–700 °C, due to the loss of PAA and OA/OLA of the organic layer of the materials.

The magnetic properties of the materials were analyzed using a vibrating sample magnetometer (VSM) in an external magnetic field ranging from −10000 Oe to 10000 Oe. The results showed that the synthesized Fe_3O_4 NPs and Fe_3O_4@Ag HNPs had a saturation magnetization value (M_s) of 60.05 emu/g and 21.5 emu/g, respectively, at 300 K (Figure 2f). The saturation magnetization value of Fe_3O_4@Ag hybrid nanoparticles is lower than that of Fe_3O_4 nanoparticles, due to the non-magnetic Ag component in the hybrid structure. However, the magnetic response of hybrid nanoparticles is relatively good, so they meet for biomedical applications.

2.2. Stability of the PAA-coated Fe_3O_4@Ag hybrid NPs

The colloidal stability of hybrid nanoparticles is very important for use as biomedical materials. It depends on several parameters of the materials such as particle size and hydro-

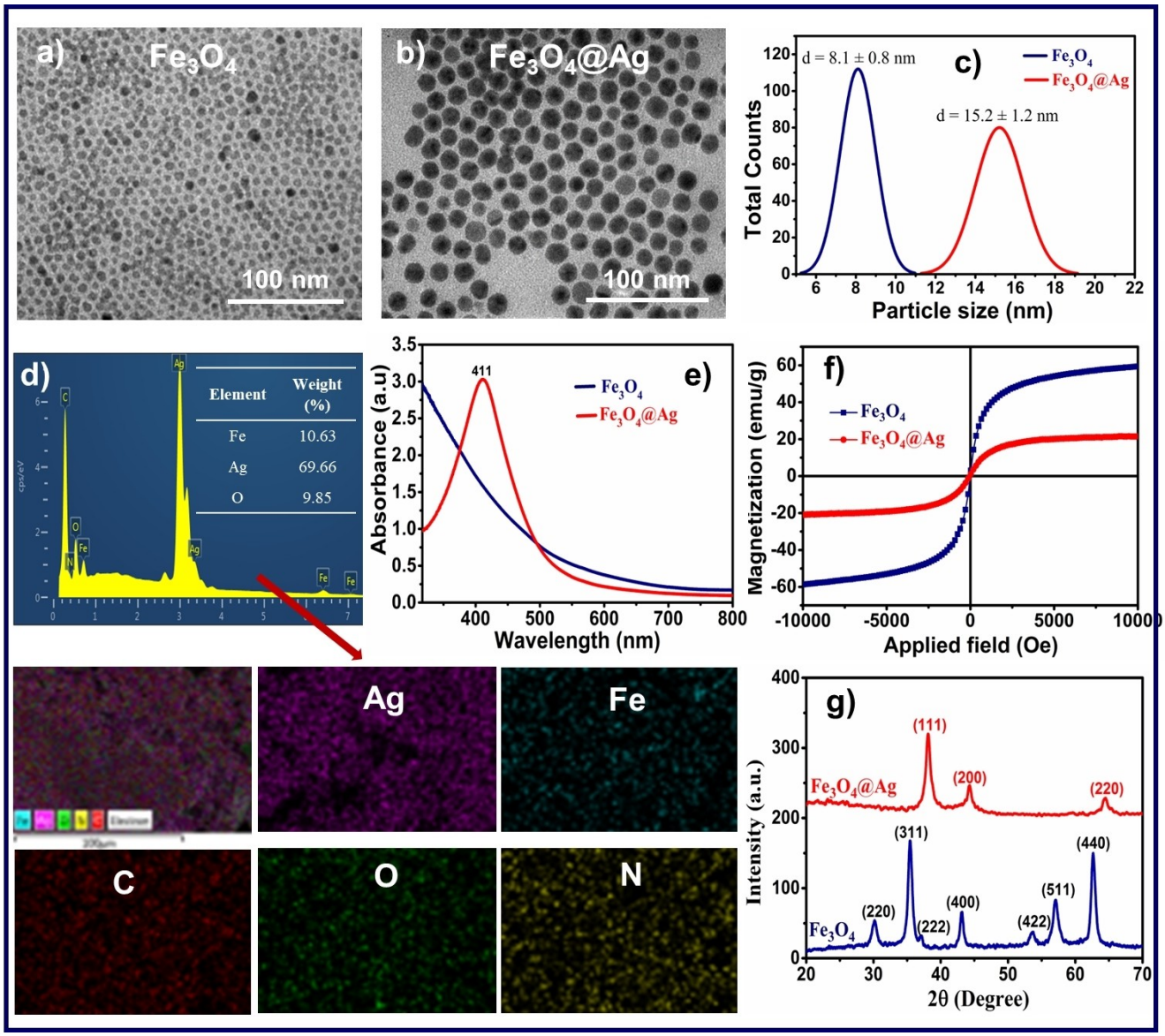

Figure 2. TEM images and the corresponding size distribution histograms of Fe_3O_4 and Fe_3O_4@Ag hybrid NPs (a-c); EDS spectra of Fe_3O_4@Ag hybrid NPs (d); UV-Vis absorption spectra of Fe_3O_4 and Fe_3O_4@Ag hybrid NPs (e); Magnetization curves of Fe_3O_4 NPs and Fe_3O_4@Ag hybrid NPs (f); and Xray diffraction pattern of the Fe_3O_4 NPs and Fe_3O_4@Ag hybrid NPs (g). (Scale bar: 100 nm).

philic property of functional groups on the surface of the nanoparticles. Under biological conditions, the stability of colloidal nanoparticles may be affected by several factors such as salinity, pH, interactions between proteins and especially enzyme activity. In this study, the effect of salt concentration and pH on the colloidal stability of the Fe_3O_4@Ag@PAA hybrid nanoparticles were examined by DLS and Zeta potential measurements. It is well known that the salt concentration in the body is maintained at about 158 mM and the pH value is around 7.3. In the present research, the colloidal stability of Fe_3O_4@Ag@PAA hybrid nanoparticles in saline at concentrations between 0 and 280 mM and pH values from 3 to 11 was evaluated. As shown in Figure 4a, when NaCl concentration is up to 200 mM, Fe_3O_4@Ag@PAA hybrid nanoparticles are well dispersed and stable in solution. When NaCl concentrations increased from 250 to 280 mM, the hybrid nanoparticles were aggregated and sedimented in solution. Similarly, the hybrid nanoparticles are colloidal stable over a wide range of pH from 4 to 11, but sedimented at pH 3 or lower (Figure 4b). The results show that Fe_3O_4@Ag@PAA hybrid nanoparticles are suitable for biomedical applications.

2.3. In vitro cytotoxicity results

The SRB assay with a range of concentration of Fe_3O_4@Ag@PAA from 5 ug/ml to 100 ug/ml was performed on Vero - a monkey kidney normal cell line, and Hep G2 - a human liver cancer cell line. Ellipticine and DMSO were used as positive and solvent

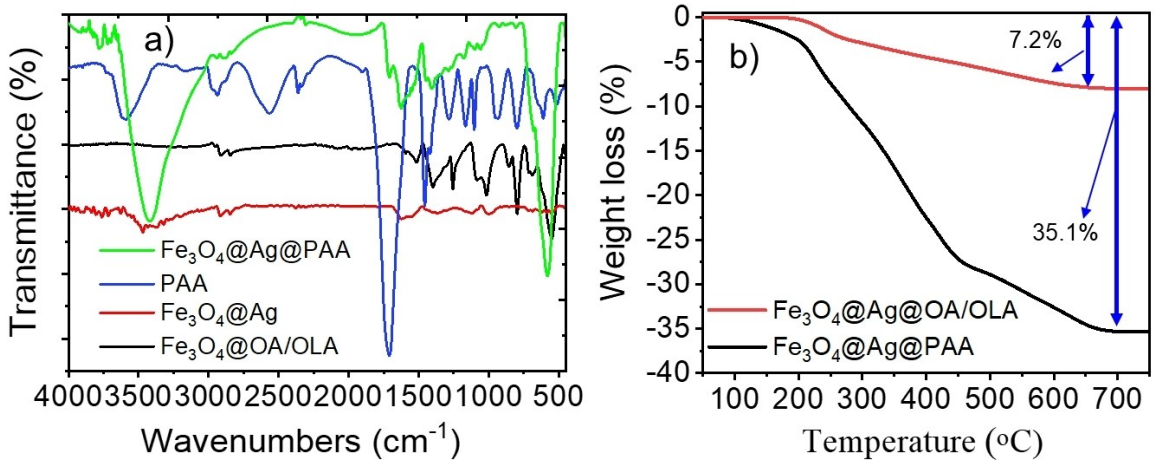

Figure 3. FT-IR spectra (a) and TGA scans (b) of OLA and of PAA encapsulated Fe_3O_4@Ag hybrid nanoparticles.

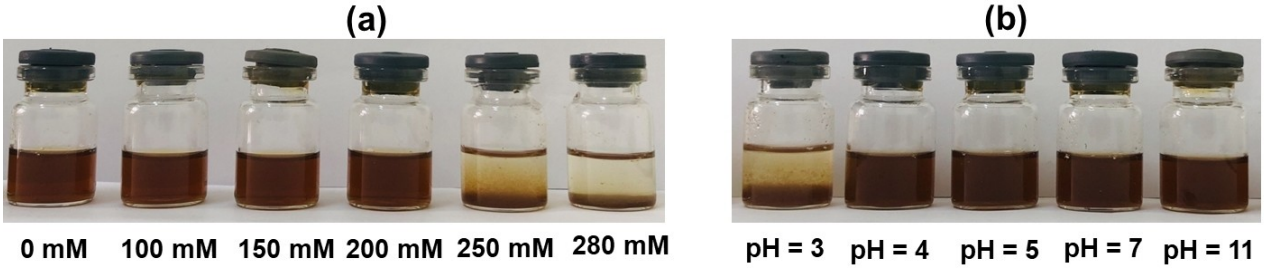

Figure 4. Photographs of the PAA encapsulated Fe_3O_4@Ag hybrid NPs in water solution under different NaCl concentrations (a) and different pH values (b). Photographs were taken on the samples after adding NaCl (a) and NaOH (b) of 2 months.

control (Figure 5a). The Fe_3O_4@Ag@PAA only exhibited cellular toxicity to Vero cells at a high concentration of 50 ug/ml with 2.5% of the cell surviving. In contrast, Hep G2 exhibited a strong response to Fe_3O_4@Ag@PAA hybrid NPs even at the concentration of 5 ug/ml with 27.54% of living cells and 100% cell death at the highest concentration of 100 ug/ml. Figure 5b indicated the significant difference in IC_{50} values of Fe_3O_4@Ag@PAA on Vero and Hep G2 with 40.3 and 8.42 ug/ml, respectively. This suggested that the combination of Ag and Fe_3O_4 NPs has selective cytotoxicity between normal and cancer cells.

(a) Cell survival rate of samples incubated with Fe_3O_4@Ag@PAA (5–10–25–50–100 ug/ml); Ellipticine (5 ug/ml) and DMSO.
(b) IC_{50} curve with log concentration of Fe_3O_4@Ag@PAA at 0.7; 1; 1.4; 1.7 and 2. Data was presented as mean ± SD. Graphs were obtained by using GraphPad and two-tailed t-test were perform to test the significant of difference of IC_{50}. $P = 0.038$ (*).

Figure 6 presented the change of cell morphology between tested concentrations. With low concentration of 5; 10; 25 ug/ml, no shape change was observed in Vero cell. When there is cell death, as the cells size decreased and the medium contained several debris from death cells, it is suggested that this material triggered the apoptosis pathway within the cell.

Previous study showed a less cytotoxicity of Fe_3O_4-Ag@PAA on both SMMC-7721 cells (human hepatocarcinoma) and L02 cells (human normal hepatocyte), with a cell viability over 90% at concentration of 60 ug/ml after 24 h of incubation.[44] In comparison, Ag-NPs was reported to have IC_{50} of 75 ug/ml on Hep G2 after 48 h exposure[45] and IC_{50} of Fe_3O_4-NPs on this cell line was more than 20 ug/ml. With at least 2.5 times lower IC_{50}, Fe_3O_4@Ag@PAA is a promising selective agent to target and kill only cancer cells without harming health tissue nearby. This effect may be attributed to cell metabolism kinetics, which is faster in cancer cells than in normal cells, thereby enhancing the intracellular release of Fe_3O_4@Ag HNPs in cancer cells. Many authors correlate the cytotoxicity and relative selectivity of nanoparticles based on Ag NPs with increased apoptosis and reduced DNA synthesis in cancer cells. The AgNPs can cross cell membranes and may interact with cellular components and organelles with ROS generation, leading to decreased antioxidant cell capacity, direct and/or indirect interaction with DNA, and apoptosis.[46–48] On this study Hep G2 was selected as it is a sensitive and regularly used cancer cell line in cytotoxicity assay. Later in vitro test would comparing the toxic of Fe_3O_4@Ag@PAA on several cancer cell lines and normal cells from different tissues. Once this information is confirmed, performing in vivo experiments to test the ability of tumor treatment would be the next stage. Moreover, the data on Vero

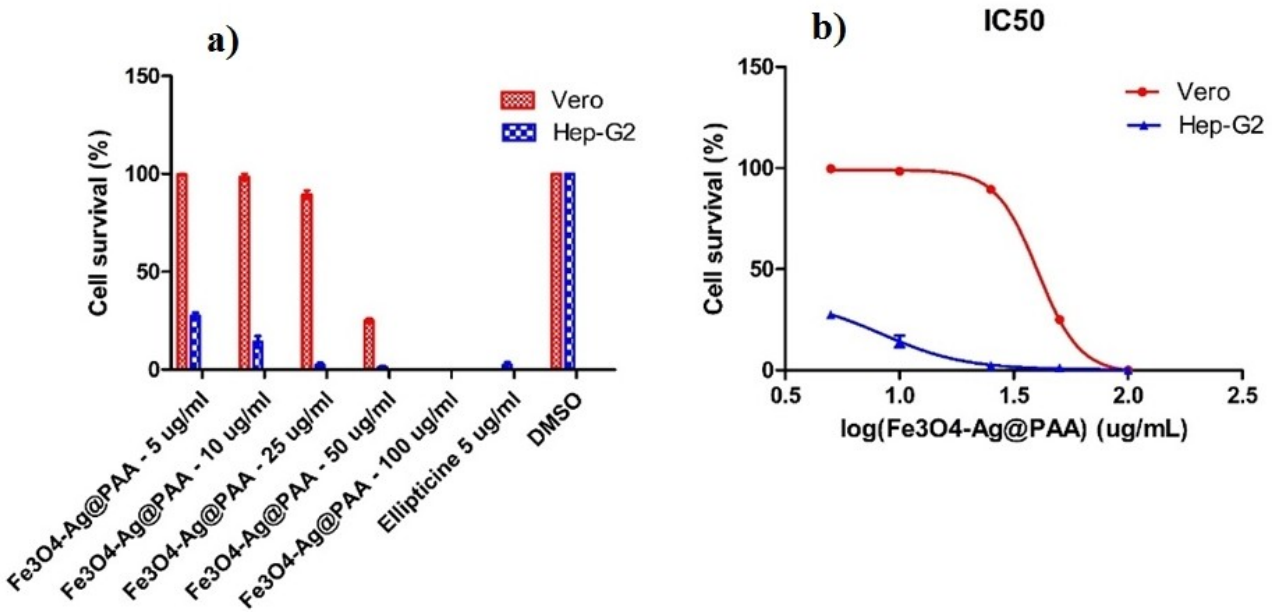

Figure 5. Cytotoxicity of Fe_3O_4@Ag@PAA on Vero and HepG2 cell lines.

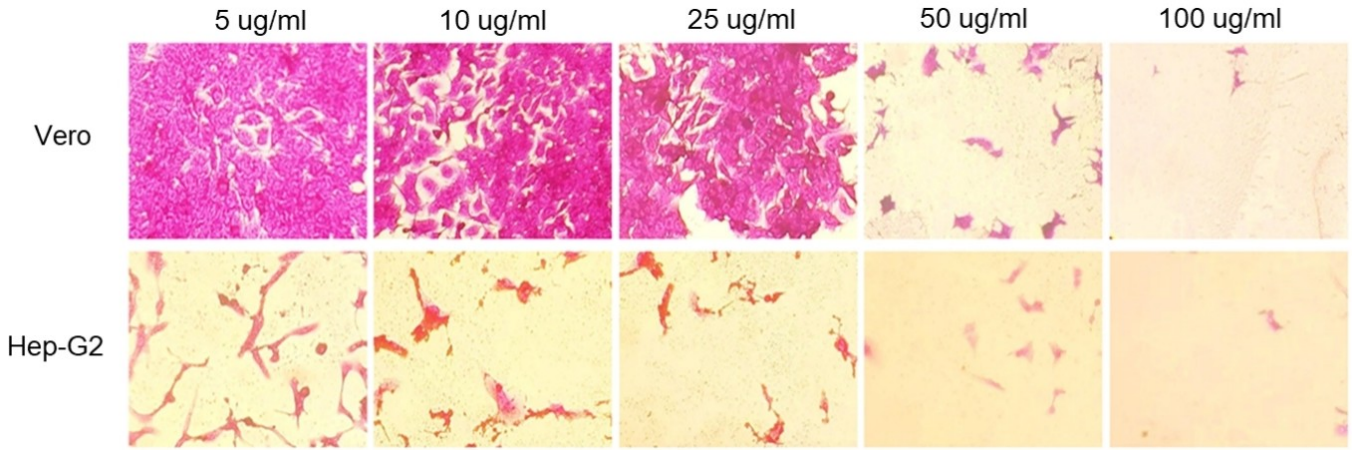

Figure 6. Vero and Hep G2 cell lines treated with different concentration of Fe_3O_4@Ag@PAA. Microscope images were taken with objective lens: 10X.

cell line proved that this material is biocompatible with normal cells, which makes it possible to apply Fe_3O_4@Ag@PAA on enhancing MRI quality.

Additionally, nanoparticles are well-known for its characteristic of inducing ROS, stimulating apoptosis and impacting cell cycle. The cellular images of Vero and Hep G2 cells placed initial clues about the same behavior of Fe_3O_4@Ag@PAA. However, further investigation should be done to better understand the properties of Fe_3O_4@Ag@PAA on cellular uptake, organ accumulation as well as mechanism of killing and targeting cancer cells.

2.4. T_2 MRI Relaxivity and X-ray Attenuation Property

The magnetization curves (Figure 3f) show that the synthesized Fe_3O_4@Ag hybrid nanoparticles maintained thesuperparamagnetic properties of Fe_3O_4@OA/OLA nanoparticles even though Ag nanoparticles were deposited on their surface. The saturation magnetization (M_s) of Fe_3O_4@OA/OLA nanoparticles is 60.05 emu/g at 300 K. After being coated with a layer of Ag nanoparticles, Ms decreased to 21.5 emu/g due to the presence of Ag. Even then, Fe_3O_4@Ag nanoparticles are still accepted as targeting agents in MRI applications, as M_s of 7–22 emu/g is commonly adopted.[49,50]

Fe_3O_4 magnetic nanoparticles are known to be used as a T_2-weighted contrast agent for MRI imaging. To demonstrate their

application to MR imaging, T_2-weighted MRI transverse relaxation of Fe_3O_4@Ag was examined (Figure 7).

Quantitative MRI imaging experiments were performed before to accurately conclude the T_2-weighted MR relaxometry value of Fe_3O_4@Ag nanoparticles in the free state. Specifically, Fe_3O_4@Ag@PAA nanoparticles with different osmolarity of iron were evaluated by MRI-weighted Spin-spin relaxation time (T_2*) with magnetic field 1.5 T (Figure 7). Accordingly, Figure 7c shows that the MRI signal intensity (negative contrast) increased with the increase of iron concentration because the superparamagnetic Fe_3O_4 nanoparticles shortened T_2* time by reducing the spin of neighboring water protons.[51] The results demonstrate that at a concentration of 0.08 mM, the negative signal intensity is the highest. ANOVA statistical analysis using SPSS software showed that for concentrations of 0.02, 0.03, 0.05 and 0.08 mM, there was a significant difference compared with the control ($p < 0.05$). The signal intensity of the obtained magnetic-optical hybrid liquid is darker than that of water when the iron concentration reaches 0.02 mM, which is lower than some Fe concentrations in Au/Ag hybrid nanoparticles reported earlier.[52,53] Figure 7c shows that transverse relaxation time inverse ($1/T_2$*) of Fe_3O_4@Ag@PAA nanoparticles is linearly correlated with iron concentration (mM). The transverse relaxation rate r_2 measurements of Fe_3O_4@Ag@PAA hybrid nanoparticles is calculated to be 139 $mM^{-1}s^{-1}$. The r_2 value is lower than that of our previously published Fe_3O_4 NPs researches,[54] which can be explained by the thick non-magnetic Ag layer coating on the magnetic Fe_3O_4 core, shields water molecules from accessing their surfaces, but is much higher than that of Fe_3O_4@Au HNPs reported in previously articles.[53,55,56] Our results suggest that the Fe3O4@Ag HNPs could be used as a good T_2-weighted MRI agent, a diagnostic time-shortening agent for MRI imaging applications.

Recent efforts to find new contrast agents in CT imaging techniques concentrated to Au NPs because of their good X-ray attenuation in comparison with common small molecule iodine compounds.[55–57] CT imaging capabilities were estimated by X-ray attenuation characteristic of the nanomaterials. The strong CT signal intensity of Au, Ag or iodine hybrid materials is mainly generated from the high X-ray absorption coefficients of gold, silver and iodine (X-ray absorption coefficient at 100 keV, Au: 5, 16 cm^2/g; I: 1.94 cm^2/g; Ag: 1.47 cm^2/g). Additionally, gold and silver atoms can produce strong X-ray attenuation due to their high density (19.32 g/cm^3 and 10.49 g/cm^3, respectively), which makes the Fe_3O_4@Ag@PAA HNPs may in the future become contrast agent ideal for computed tomography (CT) instead of conventional iodine-based contrast agents.[60,61]

Nextly, the potential to use Fe_3O_4@Ag nanoparticles as contrast agent in CT imaging was evaluated by scanning the same hybrid nanoparticle samples in the previous MRI experiment in the 128-Somatom Perspective CT scanner (Siemens), Germany). In there, the concentrations of both silver and iron samples were checked using ICP-MS. Figure 8 shows that the X-ray absorption (in Hounsfield unit) increased with the increase of Ag concentrations in a good linear relationship, and reach 129 HU at the Ag concentration of 0.06 M (Figure 8a,b). During the experimental research, it was found that the signal intensity of the CT images continuously increased without saturating, while the T_2 contrast effect of the nanoparticles saturated at a concentration of 0.08 $mmol.L^{-1}$ and no signal attenuation was observed above this concentration. This could be explained because the MRI technique is so sensitive that a sufficient T_2 contrast effect has been observed even at low concentrations. Additionally, CT compared with MRI showed lower sensitivity for the determination of small nanoparticle concentrations. This highlights the importance of our large thick-shell design, where the Ag mass is significantly higher than that of the Fe_3O_4 core (69.66 % of the respective surface mass). With our new contrast agent's core-shell system, a single nanoparticle offers the use of both MRI/CT imaging modalities, and future researches will test the effectiveness of imaging in vivo image.

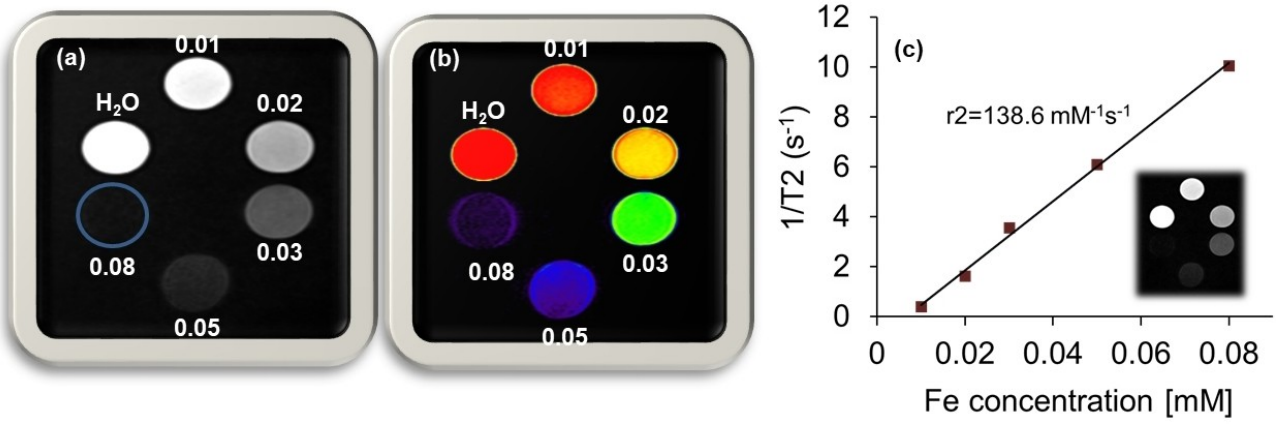

Figure 7. (a) The signal intensity; (b)T_2-weighted MRI image; (c) r_2 color maps at various concentrations of Fe_3O_4@Ag hybrid nanoparticles and plot of relaxation rate r_2 versus Fe concentration in Fe_3O_4@Ag@PAA hybrid nanostructures. The relaxivity value r_2 was obtained from the slope of the linear fitting of the experimental data (c).

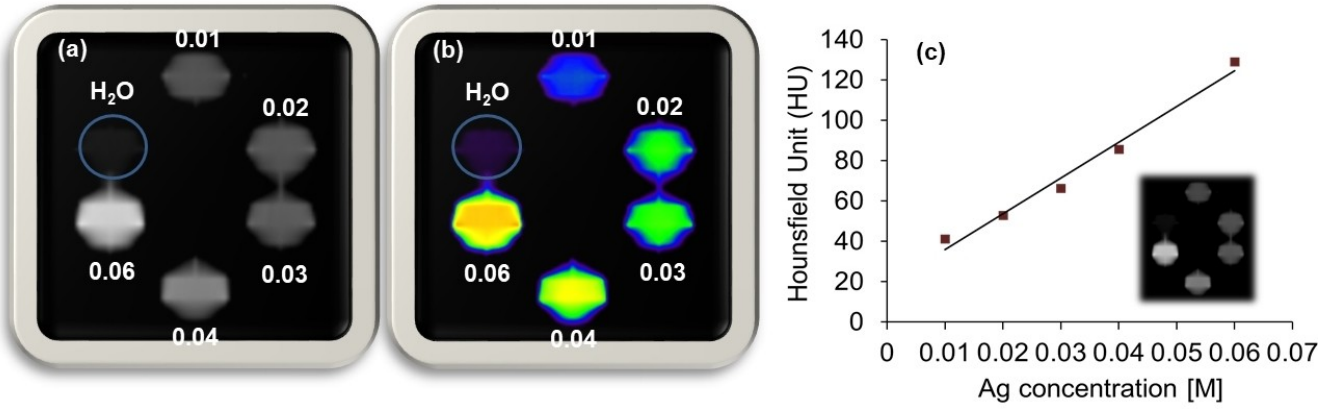

Figure 8. (a) (b) CT phantom images; (c) color maps at various concentrations of Fe_3O_4@Ag hybrid nanoparticles and (b) HU values.

3. Conclusions

In the current work, we have successfully synthesized Fe_3O_4@Ag core-shell structure hybrid nanoparticle by seeded-growth route in the thermal decomposition method, using high quality Fe_3O_4 magnetic nanoparticles as seeds. The effect of SOA ratio on the shape, size and uniformity of Fe_3O_4 seeds was studied to find the optimal conditions. The obtained Fe_3O_4@Ag HNPs hybrid nanoparticles have core-shell structure, uniform size and spherical shape, with an Ag outer shell. The hybrid nanoparticles after functionalizing the surface with polyacrylic acid (PAA) became hydrophilic and dispersed well in water. The fluid of Fe_3O_4@Ag@PAA HNPs has high stability in water media with NaCl salt concentrations above 200 mM and a wide pH range from 4 to 11. The fluid Fe_3O_4@Ag@PAA has selective cytotoxicity on Hep-G2 cancer cell lines (IC_{50} value 40.3 ug/ml for normal Vero cell lines, and 8.42 ug/ml for Hep-G2 cell lines, respectively). The results of in-vitro MRI/CT imaging showed that the value of transverse relaxation r_2 was 138.6 $mM^{-1}s^{-1}$ and good X-ray attenuation ability. These properties of the core-shell Fe_3O_4@Ag@PAA HNPs fluid may be used for multimodal MRI/CT bioimaging techniques.

Supporting Information Summary

The Supporting Information includes the detailed experimental section of this work

Conflic of Interest

Acknowledgements

Le The Tam was funded by Vingroup JSC and supported by the Postdoctoral Scholarship Programme of Vingroup Innovation Foundation (VINIF), Institute of Big Data, code VINIF.2021.STS.10.

The authors declare no conflict of interest.

Conflict of Interest

The authors declare no conflict of interest.

Data Availability Statement

The data that support the findings of this study are available from the corresponding author upon reasonable request.

Keywords: Dual-mode MR/CT imaging applications · cytotoxicity · imaging agents · nanostructures · poly(acrylic) acid (PAA)

[1] B. Fischl, A. M. Dale, *Biological Science.* **2015**, *97*, 11050–11055.
[2] N. Gogtay, J. N. Giedd, L. Lusk, K. M. Hayashi, D. Greenstein, A. C. Vaituzis, T. F. Nugent, D. H. Herman, L. S. Clasen, A. W. Toga, J. L. Rapoport, P. M. Thompson, *Biological Science.* **2004**, *97*, 8174–8179.
[3] J. Xian, M. Chen, Z. Jin, *Chin. Med. J.* **2015**, *128*, 569–570.
[4] S. Kakeda, Y. Korogi, *Neuroradiology.* **2010**, *52*, 711–721.
[5] C. F. G. C. Geraldes, S. Laurent, *Contrast Media Mol. Imaging* **2009**, *4*, 1–23.
[6] B. Hyon, B. Na, I. C. Song, T. Hyeon, *Adv. Mater.* **2009**, *21*, 2133–2148.
[7] M. J. Alizadeh, H. Kariminezhad, A. S. Monfared, A. Mostafazadeh, H. Amani, F. Niksirat, R. Pourbagher, *Mater. Res. Express.* **2019**, *6*, 065025–065038.
[8] P. Caravan, J. J. Ellison, T. J. McMurry, R. B. Lauffer, *Chem. Rev.* **1999**, *99*, 2293–352.
[9] D. H. Kim, S. H. Choi, S. Y. Kim, M. J. Kim, S. S. Lee, J. H. Byun, *Radiology.* **2019**, *291*, 651–657.
[10] P. Hermann, J. Kotek, V. Kubíček, I. Lukeš, *Dalton Trans.* **2008**, *9226*, 3027–3047.
[11] L. Gao, J. Zhou, J. Yu, Q. Li, X. Liu, L. Sun, T. Peng, J. Wang, J. Zhu, J. Sun, W. Lu, Lei Yu, Z. Yan, Y. Wang, *Sci. Rep.* **2017**, *7*, 1–13.
[12] Y. D. Xiao, R. Paudel, J. Liu, C. Ma, Z. S. Zhang, S. K. Zhou, *Int. J. Mol. Med.* **2016**, *38*, 1319–1326.
[13] H. S. Thomsen, *Eur. Radiol.* **2006**, *16*, 2619–2621.
[14] D. J. Todd, J. Kay, *Annu. Rev. Med.* **2016**, *67*, 273–291.
[15] P. Marckmann, L. Skov, K. Rossen, A. Dupont, M. B. Damholt, J. G. Heaf, H. S. Thomsen, *J. Am. Soc. Nephrol.* **2006**, *17*, 2359–2362.
[16] Pharmacovigilance Risk Assessment Committee, *European Medicines Agency.* **2017**.
[17] J. G. Penfield, R. F. Reilly, *Nat. Clin. Pract. Nephrol.* **2007**, *3*, 654–668.
[18] J. F. Hainfeld, D. N. Slatkin, T. M. Focella, H. M. Smilowitz, *Br. J. Radiol.* **2006**, *79*, 248–253.
[19] C. Peng, L. Zheng, Q. Chen, M. Shen, R. Guo, H. Wang, X. Cao, G. Zhang, X. Shi, *Biomaterials.* **2012**, *33*, 1107–1119.

[20] Q. Chen, K. Li, S. Wen, H. Liu, C. Peng, H. Cai, M. Shen, G. Zhang, X. Shi, *Biomaterials.* **2013**, *34*, 5200–5209.
[21] H. Liu, Y. Xu, S. Wen, Q. Chen, L. Zheng, Mingwu Shen, J. Zhao, G. Zhang, X. Shi, *Chem. A Eur. J.* **2013**, *19*, 6409–6416.
[22] P. S. Miedema, *Raman Spectroscopy with X-Rays*, pub. intech, **2017**, 226.
[23] B. Mruk, *Polish J. Radiol.* **2016**, *81*, 157–165.
[24] S. M. Park, A. Aalipour, O. Vermesh, J. H. Yu, S. S. Gambhir, *Nat. Rev. Mater.* **2017**, *2*, 17014.
[25] L. T. Tam, N. H. Du, N. T. N. Linh, N. T. Vuong, P. T. H. Tuyet, N. T. H. Hoa, N. Q. Thang, H. T. Ha, D. T. Chien, B. L. Minh, L. T. Lu, L. D. Duong, S. V. Bhosale, T. D. Lam, *J. Nanosci. Nanotechnol.* **2020**, *20*, 5338–5348.
[26] V. T. K. Oanh, L. T. Tam, D. H. Doan, N. X. Truong, N. X. Ca, V. T. Thu, L. T. Lu, T. D. Lam, *Mater. Chem. Phys.* **2020**, *245*, 122762.
[27] V. T. K. Oanh, T. D. Lam, V. T. Thu, L. T. Lu, P. H. Nam, L. T. Tam, D. H. Manh, N. X. Phuc, *J. Electron. Mater.* **2016**, *45*, 4010–4017.
[28] J. S. Kim, E. Kuk, K. N. Yu, J. Kim, S. J. Park, H. J. Lee, S. H. Kim, Y. K. Park, Y. H. Park, Ch. Hwang, Y. Kim, Y. Lee, D. Jeong, M. Cho, *Nanomedicine Nanotechnology, Biol. Med.* **2007**, *3*, 95–101.
[29] S. Galdiero, A. Falanga, M. Vitiello, M. Cantisani, V. Marra, M. Galdiero, *Molecules.* **2011**, *16*, 8894–8918.
[30] S. H. Lee, B. H. Jun, *Int. J. Mol. Sci.* **2019**, *20*, 1–24.
[31] M. Sabela, S. Balme, M. Bechelany, J. M. Janot, K. Bisetty, *Adv. Eng. Mater.* **2017**, *19*, 1700270(1–24).
[32] S. Ramesh, M. Grijalva, A. Debut, B. G. De La Torre, F. Albericio, L. H. Cumbal, *Biomater. Sci.* **2016**, *4*, 1713–1725.
[33] J. Bussink, J. H. A. M. Kaanders, W. T. A. Van Der Graaf, W. J. G. Oyen, *Nat. Rev. Clin. Oncol.* **2011**, *8*, 233–242.
[34] J. Garcia, T. Tang, A. Y. Louie, *Nanomedicine.* **2015**, *10*, 1343–1359.
[35] S. He, N. J. J. Johnson, V. A. N. Huu, E. Cory, *Nano Lett.* **2017**, *17*, 4873–4880.
[36] W. Feng, X. J. Zhou, W. Nie, L. Chen, K. X. Qiu, Y. Z. Zhang, C. L. He, *ACS Appl. Mater. Interfaces.* **2015**, *7*, 4354–4367.
[37] M. A. Dheyab, A. A. Aziz, M. S. Jameel, O. A. Noqta, P. M. Khaniabadi, B. Mehrdel, *Mater. Today Commun.* **2020**, *25*, 101368.
[38] L. Zhang, S. Tong, Q. Zhang, G. Bao, *ACS Appl. Nano Mater.* **2020**, *3*, 6785–6797.
[39] S. Parka, H. Kima, S. C. Lima, K. Lima, E. S. Leeb, K. T. Ohc, H. G. Choid, Y. S. Youn, *J. Controlled Release* **2019**, *304*, 7–18.
[40] R. G. Charles, M. A. Pawlikowski, *J. Phys. Chem.* **1958**, *62*, 440–444.
[41] N. Bao, L. Shen, Y. Wang, P. Padhan, A. Gupta, *J. Am. Chem. Soc.* **2007**, *129*, 12374–12375.
[42] Y. Yin, A. P. Alivisatos, *Nature.* **2005**, *437*, 664–670.
[43] L. T. Lu, N. T. Dung, L. D. Tung, C. T. Thanh, O. K. Quy, Ng. V. Chuc, S. Maenosono, N. T. K. Thanh, *Nanoscale.* **2015**, *7*, 19596–19610.
[44] Q. Ding, D. Liu, D. Guo, F. Yang, X. Pang, R. Che, N. Zhou, J. Xie, J. Sun, Z. Huang, N. Gu, *Biomaterials.* **2017**, *124*, 35–46.
[45] E. Ahmadian, S. M. Dizaj, E. Rahimpour, *Mater. Sci. Eng. C.* **2017**, *93*, 465–471.
[46] Y. Xue, T. Zhang, B. Zhang, F. Gong, Y. Huang, M. Tang, *J. Appl. Toxicol.* **2016**, *36*, 352–360.
[47] M. Jeyaraj, G. Sathishkumar, G. Sivanandhan, D. MubarakAli, M. Rajesh, R. Arun, G. Kapildev, M. Manickavasagam, N. Thajuddin, K. Premkumar, *Colloids Surf. B* **2013**, *106*, 86–92.
[48] R. R. Palem, S. D. Ganesh, Z. Kronekova, M. Sláviková, N. Saha, P. Saha, *Bull. Mater. Sci.* **2018**, *41*, 1–11.
[49] P. Tartaj, C. J. Serna, *J. Am. Chem. Soc.* **2003**, *125*, 15754–15755.
[50] H. Lu, G. Yi, S. Zhao, D. Chen, L. H. Guo, J. Cheng, *J. Mater. Chem.* **2004**, *14*, 1336–1341.
[51] N. Nasongkla, E. Bey, J. Ren, *Nano Lett.* **2006**, *6*, 2427–2430.
[52] J. H. Park, G. V. Maltzahn, L. Zhang, *Adv. Mater.* **2008**, *20*, 1630–1635.
[53] H. N. Du, L. T. Tam, T. N. N. Linh, P. T. H. Tuyet, H. D. Quang, N. T. Vuong, L. T. Lu, T. D. Lam, *ChemistrySelect.* **2021**, *6*, 9389–9398.
[54] L. T. Tam, H. N. Du, T. N. N. Linh, P. T. H. Tuyet, H. D. Quang, N. T. Vuong, L. T. T. Hiep, V. T. K. Oanh, L. H. Khoa, L. D. Duong, L. T. Lu, T. D. Lam, *ChemistrySelect.* **2020**, *5*, 12915–12923.
[55] L. S. Lin, X. Yang, Z. Zhou, *Adv. Mater.* **2017**, *29*, 1606681 (1–9).
[56] H. Ittrich, K. Peldschus, N. Raabe, M. Kaul, G. Adam, *RoFo Fortschritte auf dem Gebiet der Rontgenstrahlen und der Bildgeb. Verfahren.* **2013**, *185*, 1149–1166.
[57] D. Xi, S. Dong, X. Meng, Q. Lu, L. Meng, J. Ye, *RSC Adv.* **2012**, *2*, 12515–12524.
[58] L. Kong, C. S. Alves, W. Hou, *ACS Appl. Mater. Interfaces.* **2015**, *7*, 4833–4843.
[59] Y. C. Dong, M. Hajfathalian, P. S. N. Maidment, *Sci. Rep.* **2019**, *9*, 14912(1–13).
[60] E. M. Lee, J. Lee, Y. Kim, *ACS Biomater. Sci. Eng.* **2020**, *6*, 4390–4396.
[61] Z. Li, L. Tian, J. Liu, *Adv. Healthcare Mater.* **2017**, *6*, 1700413(1–11).

Submitted: April 8, 2022
Accepted: June 10, 2022